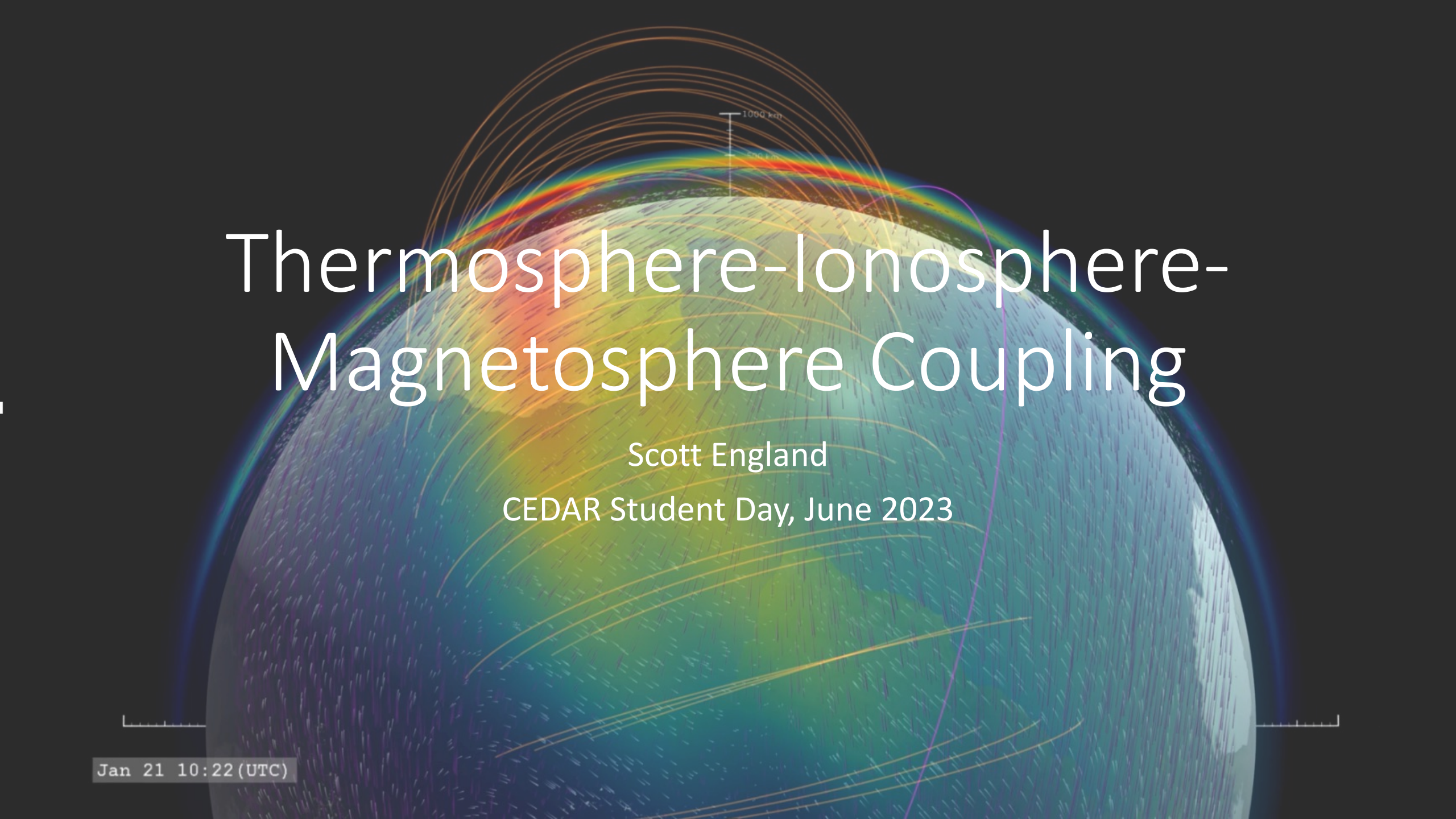

Thermosphere-Ionosphere-Magnetosphere Coupling

Scott England

CEDAR Student Day, June 2023

Outline

1. Energy inputs and energy flow
2. Relationship of ions and neutrals
3. Neutral composition impacts on the ionosphere
4. Neutral wind impacts on the ionosphere
5. Ionospheric impacts on the neutral atmosphere
6. Magnetospheric impacts on the ionosphere & thermosphere

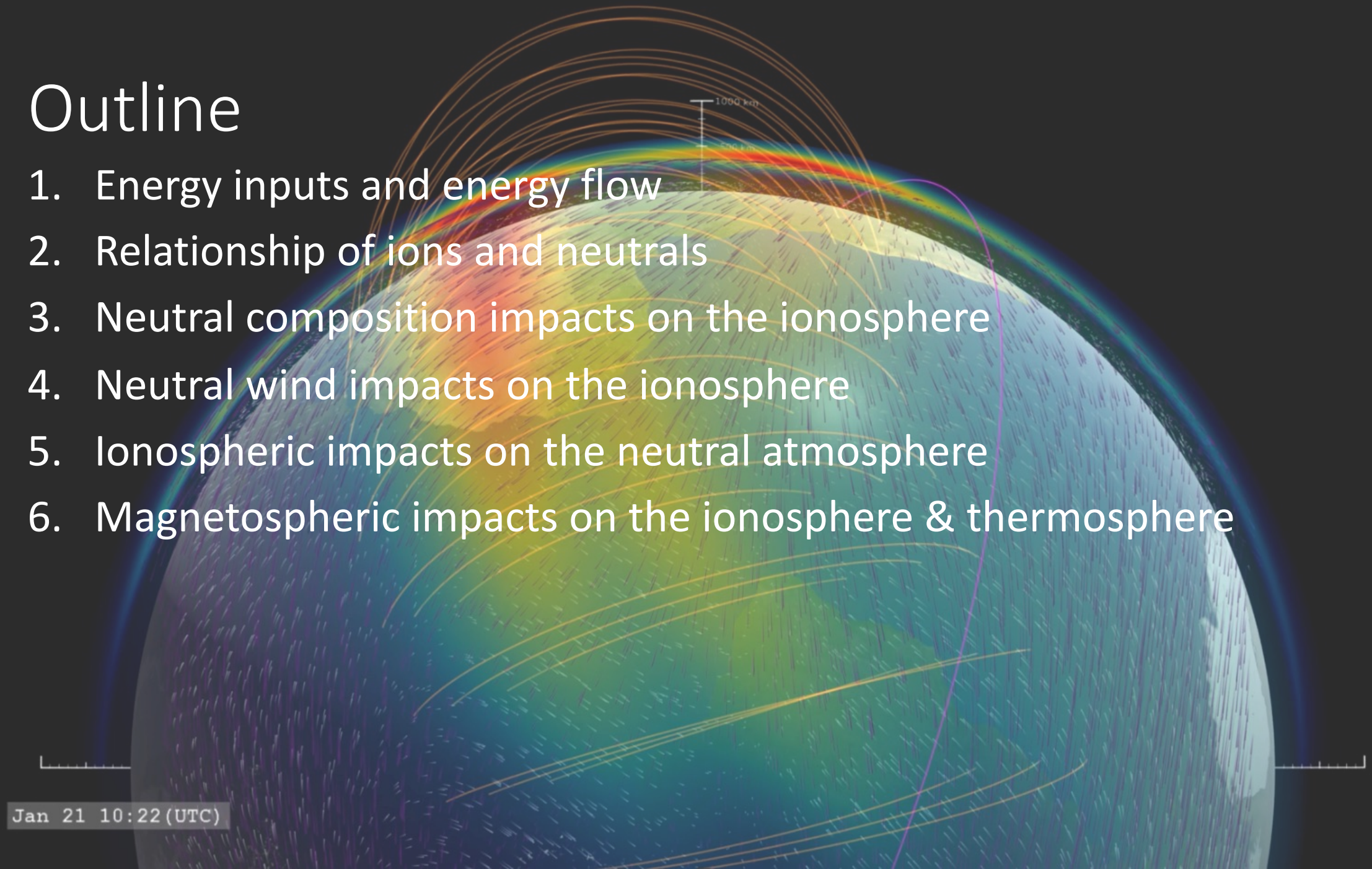

Energy inputs and energy flow

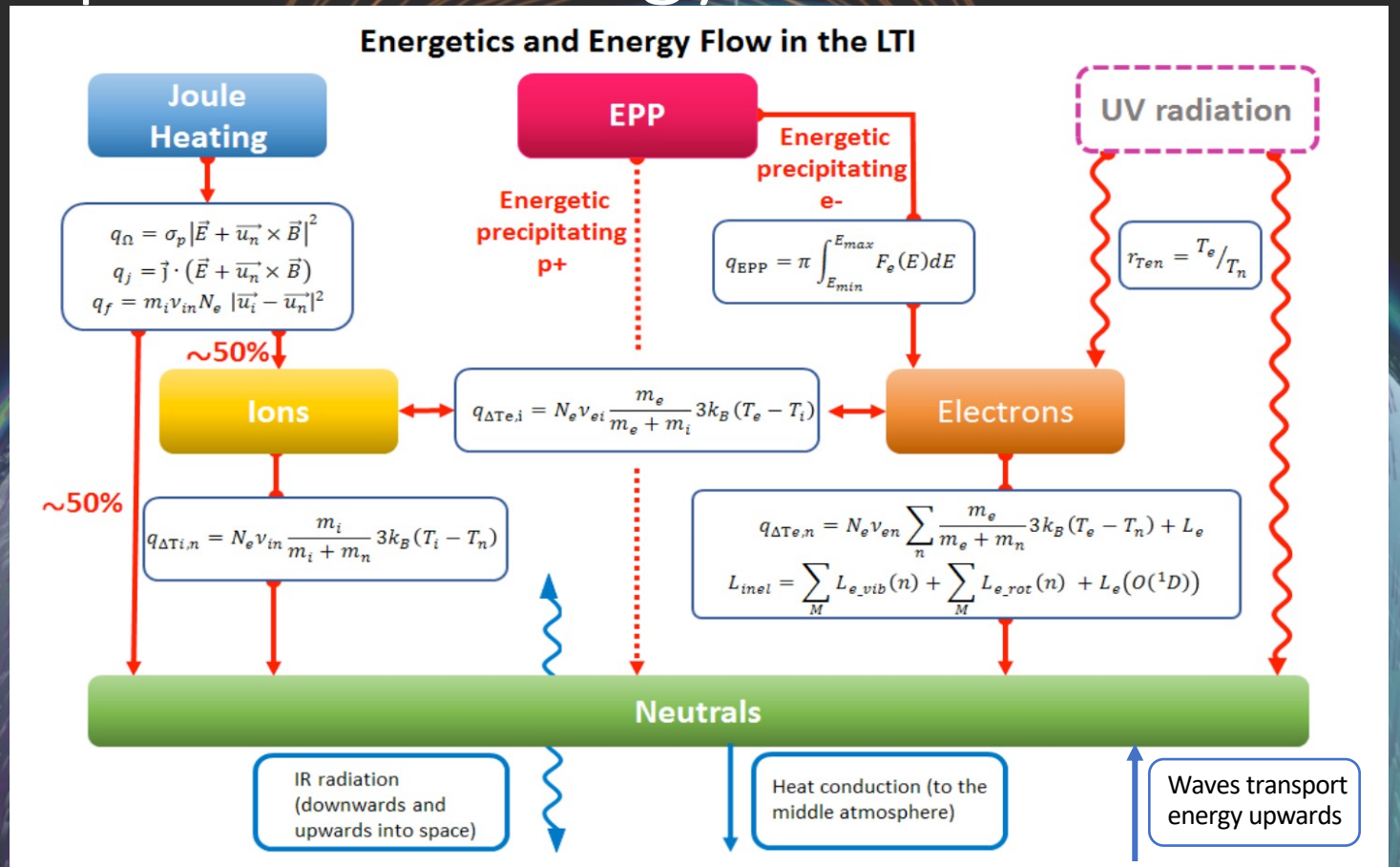

Figure 9 Flow chart of LTI energetics showing Ohmic heating rate (q_Ω), Joule heating rate (q_j), frictional heating rate (q_f), heating rate due to energetic particle precipitation (q_{EPP}), and heat transfer rates between ions and neutrals ($q_{\Delta Ti,n}$), between electrons and neutrals ($q_{\Delta Te,n}$), and between electrons and ions ($q_{\Delta Te,i}$), as well as electron energy dissipation through vibrational, rotational and quantum state excitation of LTI constituents (L_{inel}) [figure: T. Sarris, S. Buchert]

Relationship of ions and neutrals

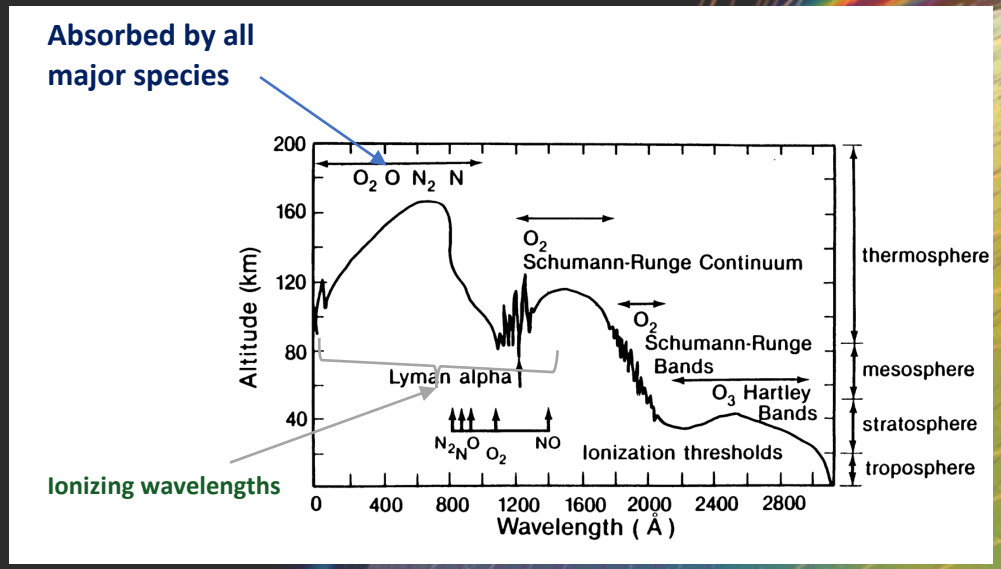

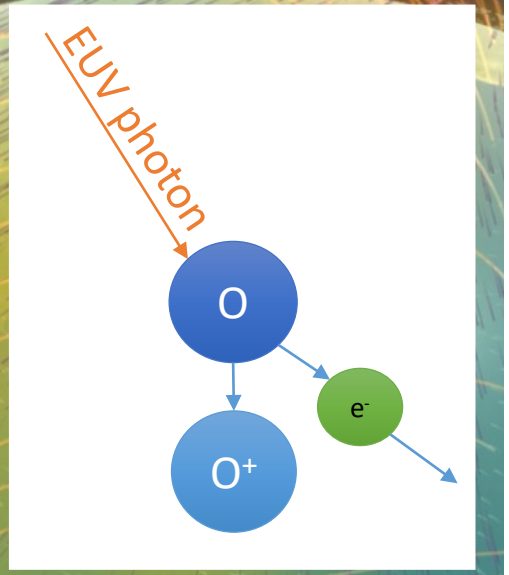

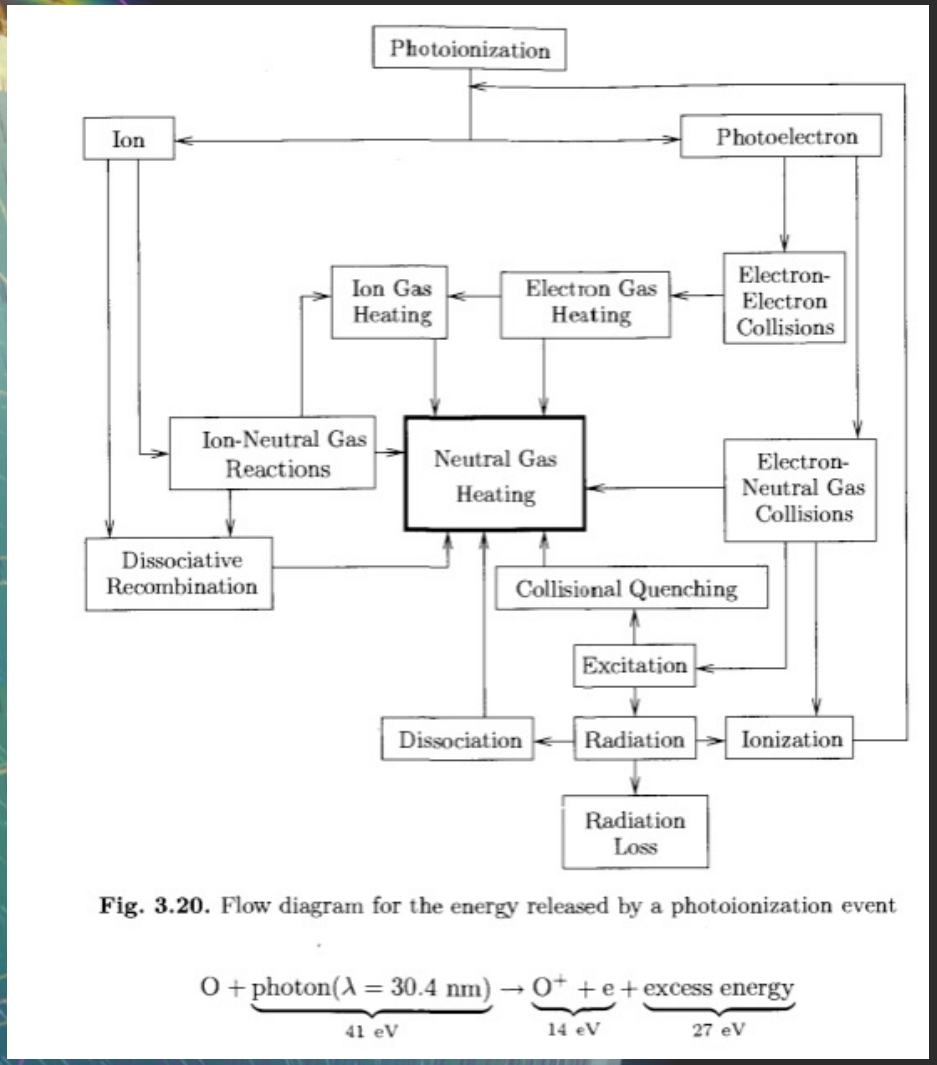

Fig. 3.20. Flow diagram for the energy released by a photoionization event

$$\mathrm{O} + \underbrace{\mathrm{photon}(\lambda = 30.4\ \mathrm{nm})}_{41\ \mathrm{eV}} \rightarrow \underbrace{\mathrm{O}^+ + \mathrm{e}}_{14\ \mathrm{eV}} + \underbrace{\mathrm{excess\ energy}}_{27\ \mathrm{eV}}$$

$O + photon\ (\lambda \leq 91\ nm) \rightarrow O^+ + e^-$

$O_2 + photon\ (\lambda \leq 103\ nm) \rightarrow O_2^+ + e^-$
or $O + O^+ + e^-$

$N_2 + photon\ (\lambda \leq 80\ nm) \rightarrow N_2^+ + e^-$

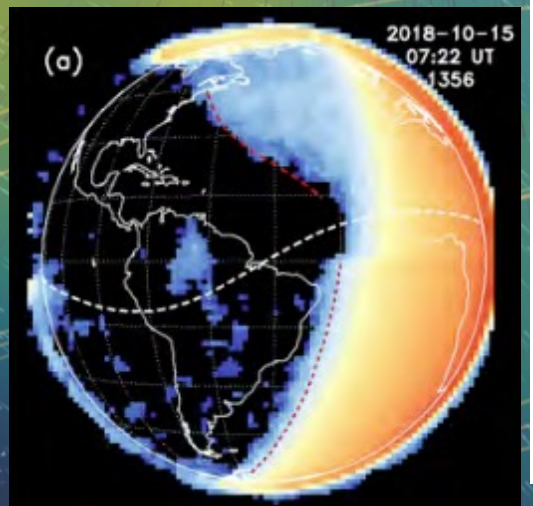

Jan 21 10:22(UTC)

Neutral composition impacts on the ionosphere

- O^+ production
  - O + photon -> $O^+ + e^-$
  - O_2 + photon -> $O + O^+ + e^-$
- O^+ loss
  - $O^+ + N_2$ -> $NO^+ + N$

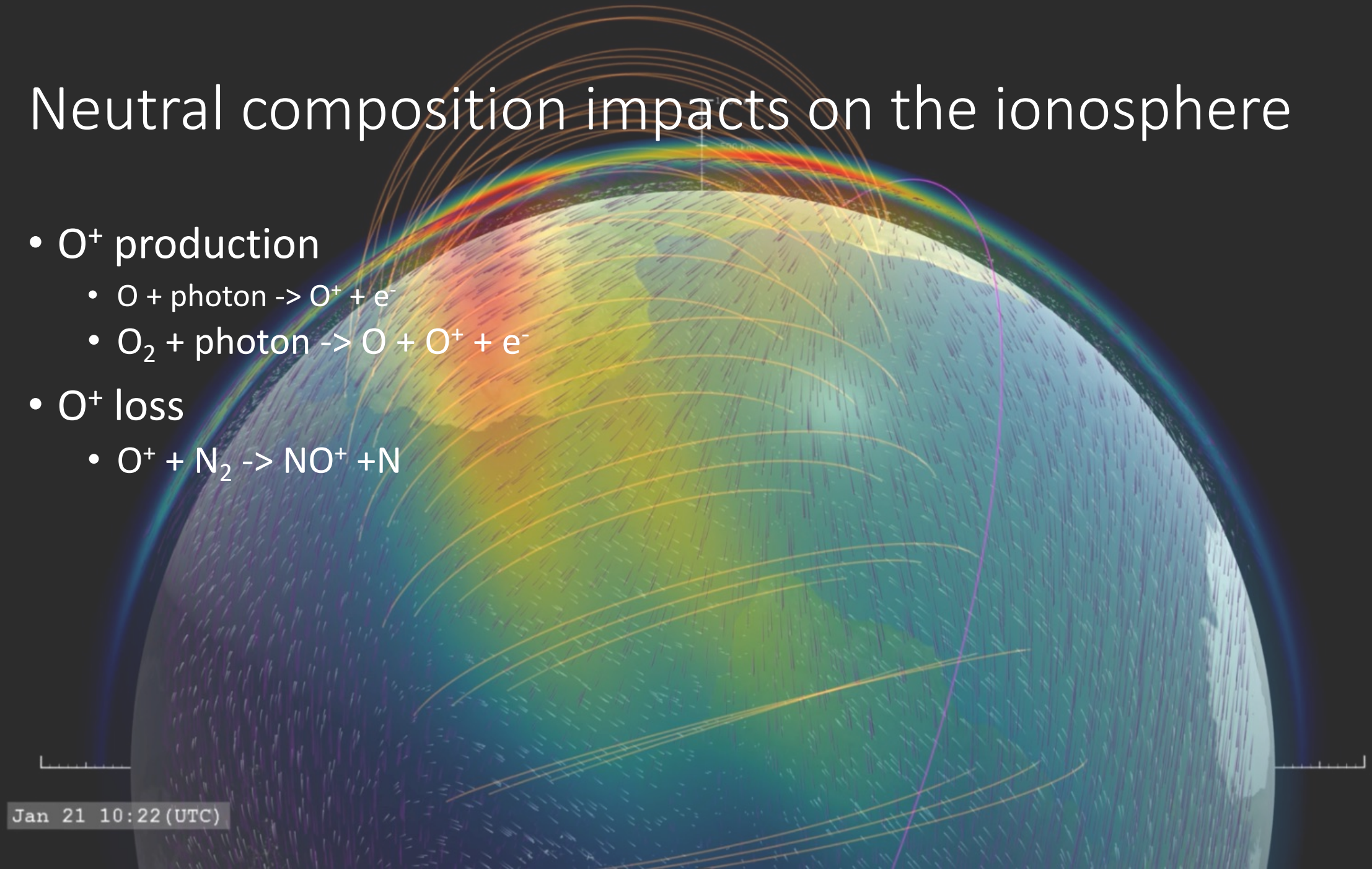

Neutral wind impacts on the ionosphere

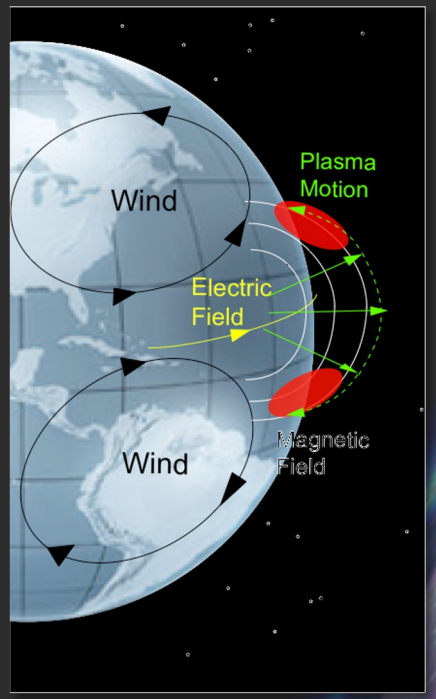

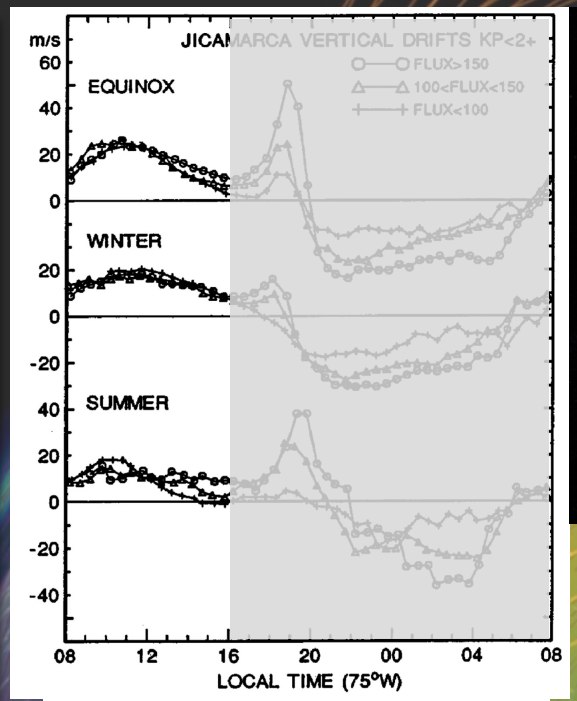

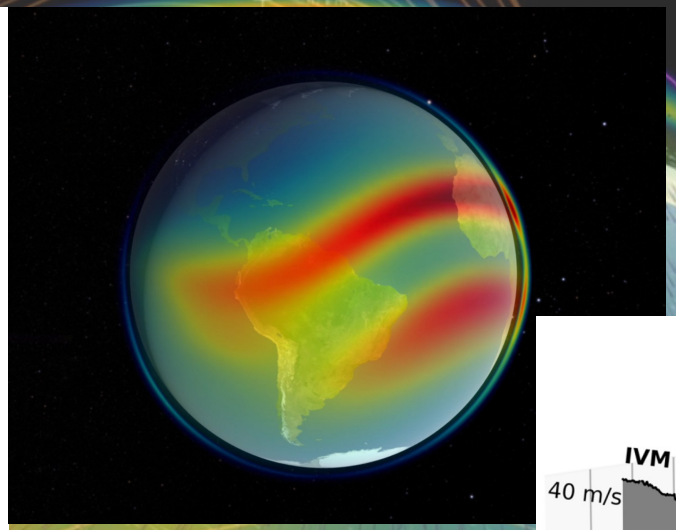

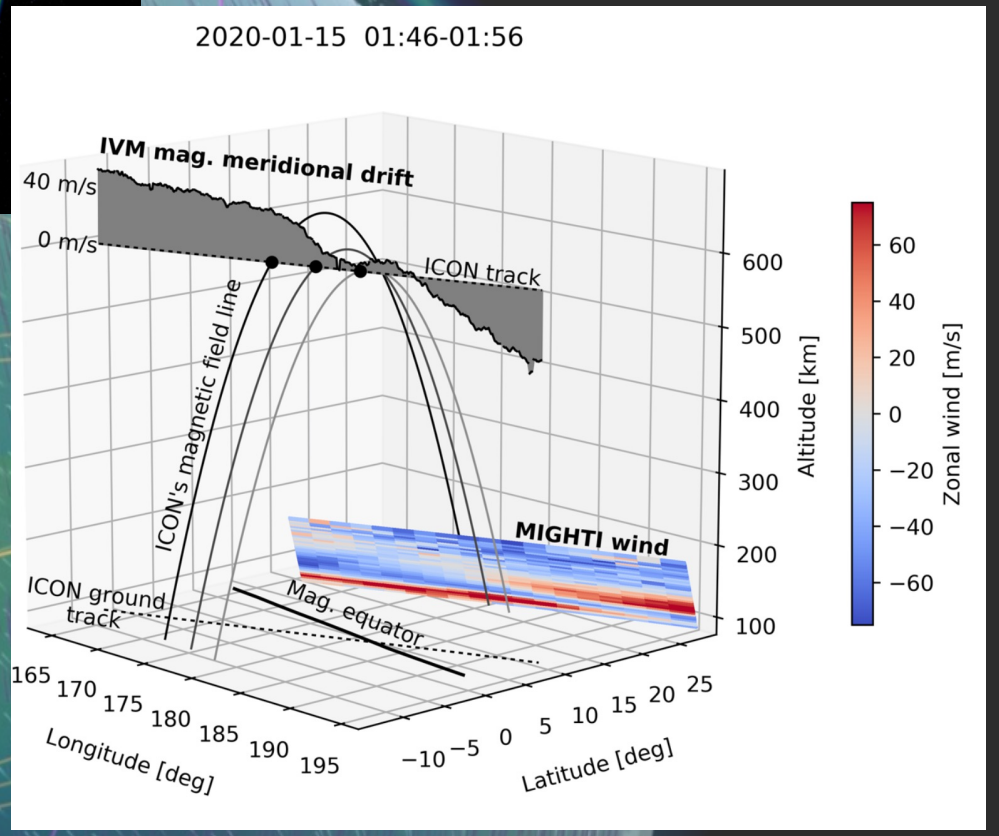

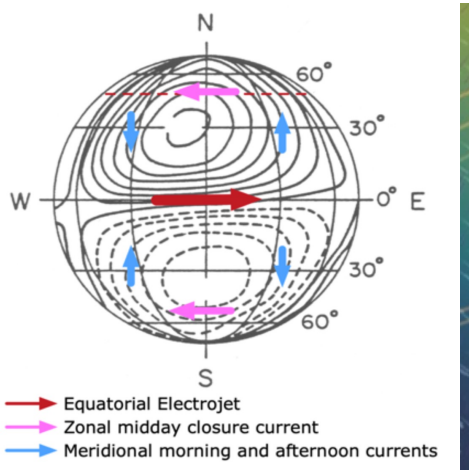

Jan 21 10:22(UTC)

Neutral wind impacts on the ionosphere

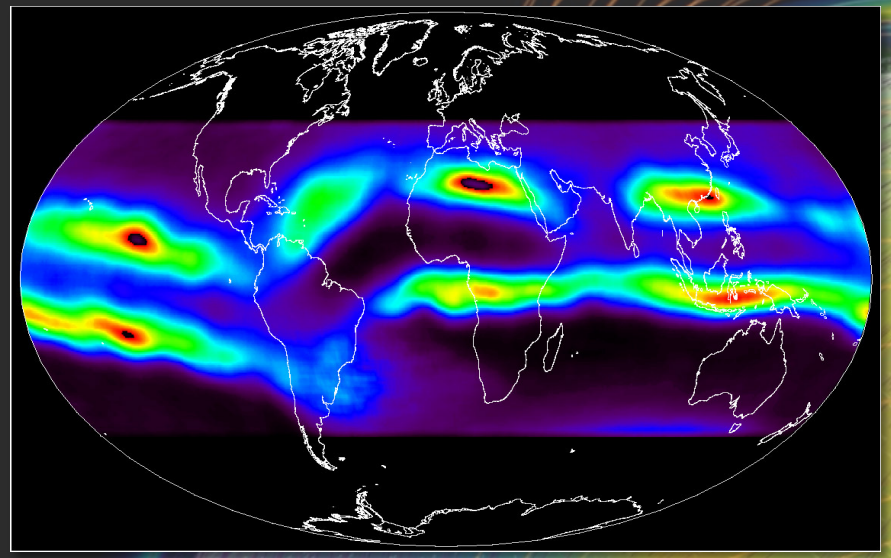

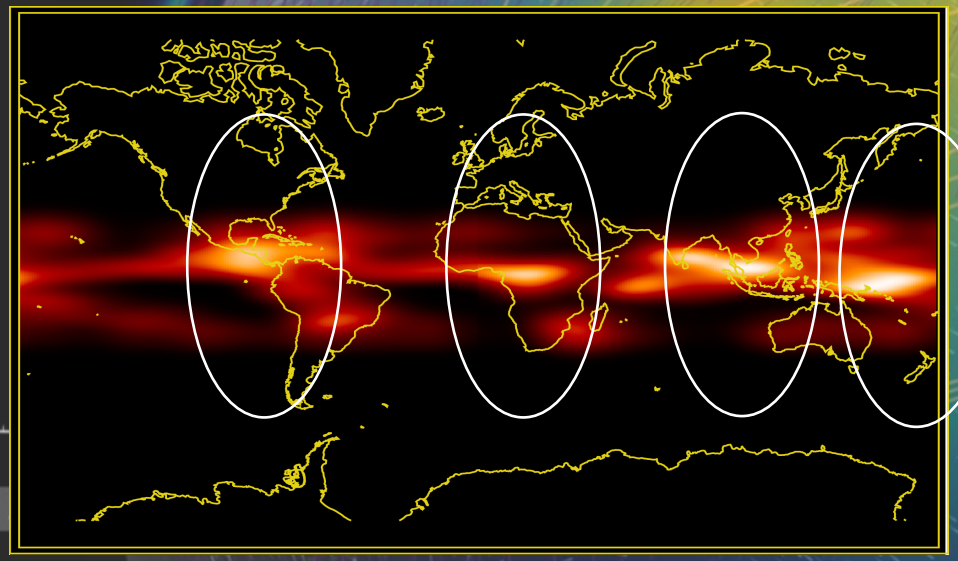

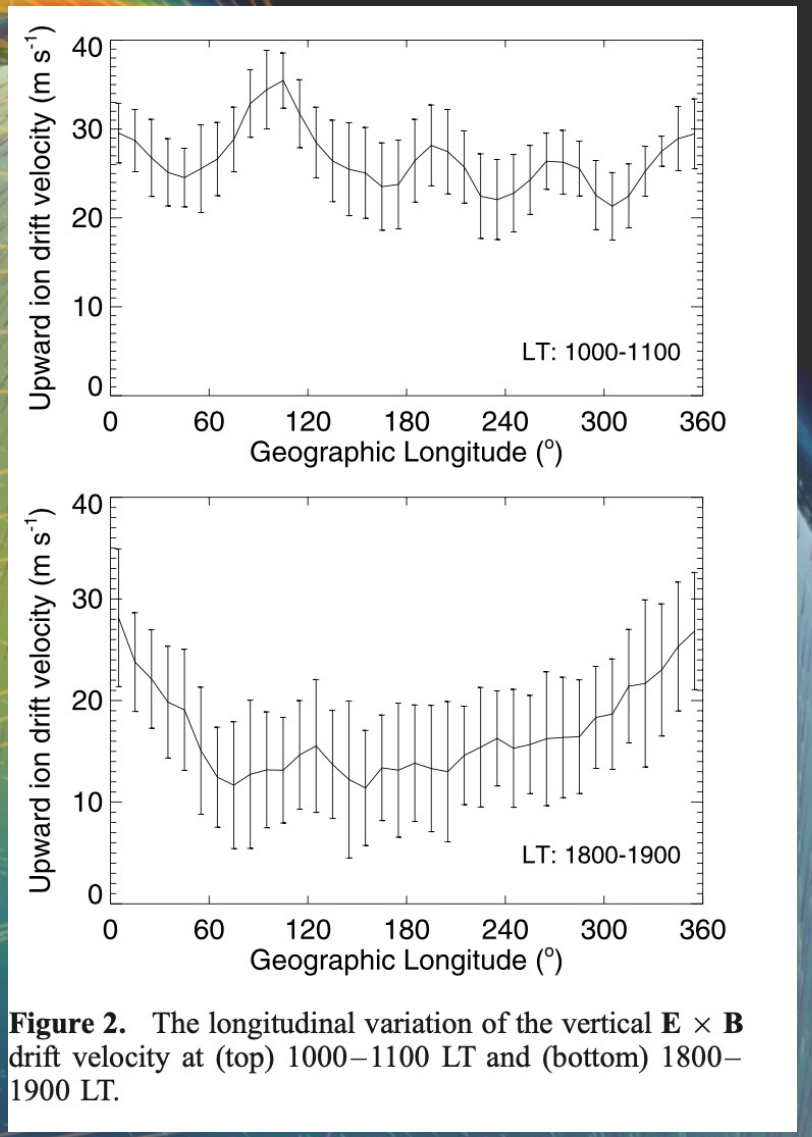

Figure 2. The longitudinal variation of the vertical **E** × **B** drift velocity at (top) 1000–1100 LT and (bottom) 1800–1900 LT.

Jan

Neutral wind impacts on the ionosphere

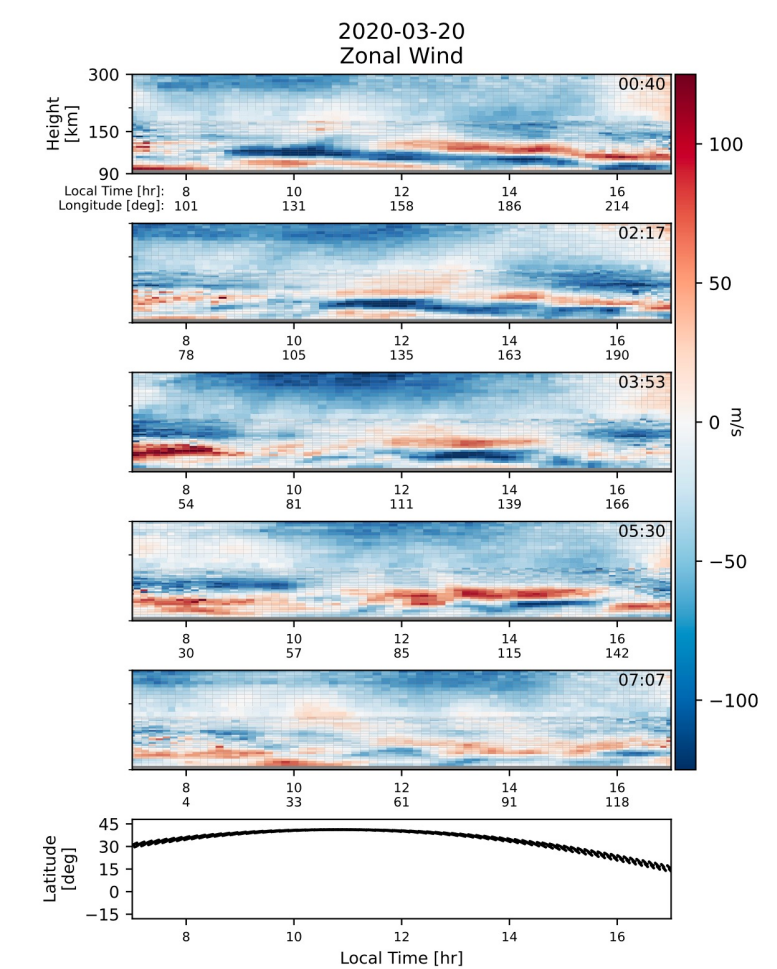

Figure 1. Daytime zonal winds observed with ICON Michelson Interferometer for Global High-Resolution Thermospheric Imaging on five successive orbits from 20 March 2020. Values are shown as functions of altitude and local time. The latitude of the wind observations at 90 km altitude is shown in the bottom panel. The time at the middle of each dayside orbit segment in UTC is noted.

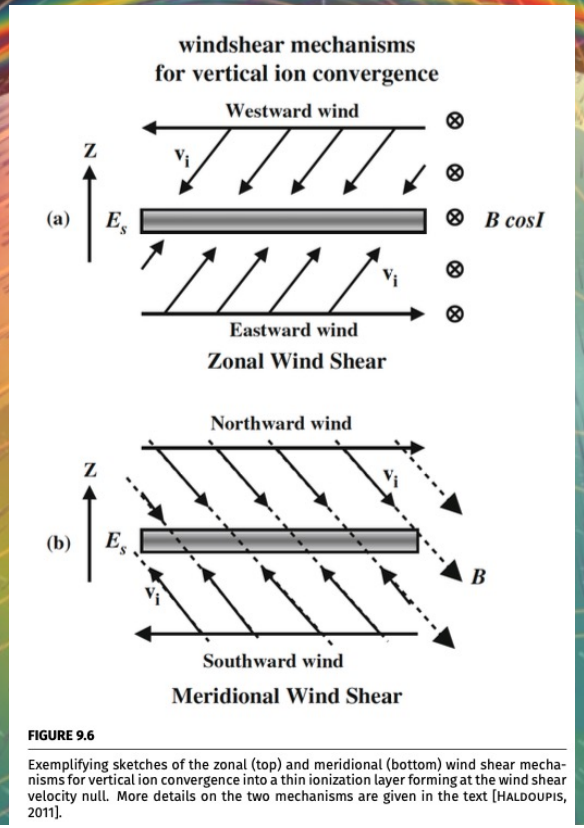

FIGURE 9.6

Exemplifying sketches of the zonal (top) and meridional (bottom) wind shear mechanisms for vertical ion convergence into a thin ionization layer forming at the wind shear velocity null. More details on the two mechanisms are given in the text [HALDOUPIS, 2011].

$$w_i = \frac{1}{1+r^2}\left(rU_m \cos I - V_m \cos I \sin I\right)$$

$$r = \frac{\nu_i}{\Omega_i},$$

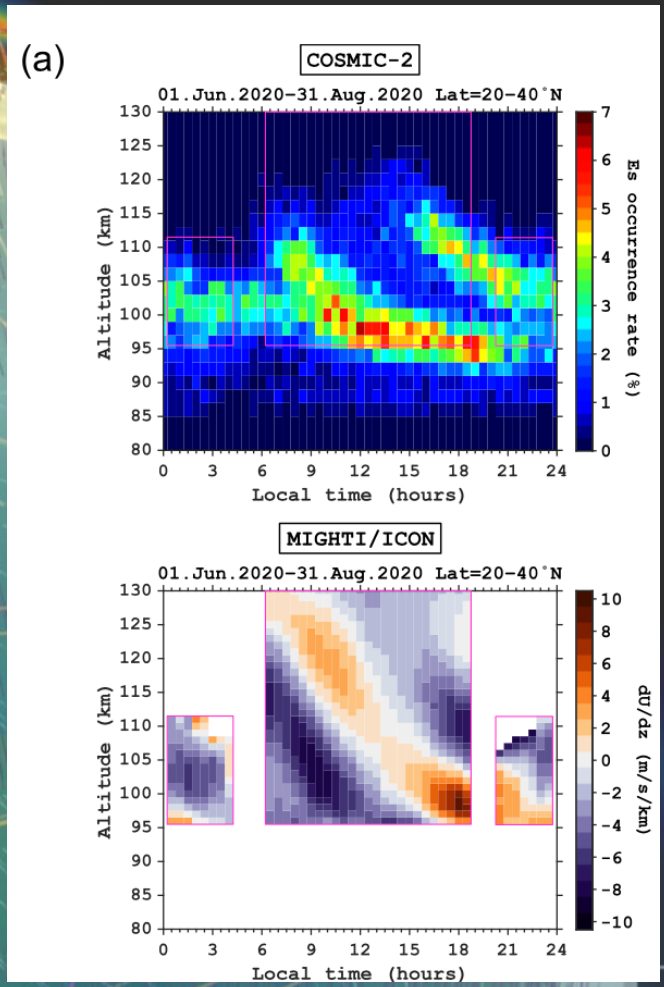

Ionospheric impacts on the neutral atmosphere

$$Collisional\ Heating: q_{coll} = A(T_i - T_n) + B(T_e - T_n)$$

$$Acceleration: \rho\frac{D\vec{u}}{Dt} = -\nabla p + \eta\frac{\partial^2 u}{\partial z^2} + \rho\vec{g} + \rho\upsilon_{n,i}(\vec{u}_i - \vec{u}) + 2\rho\vec{u}\times\vec{\Omega}_E$$

Equatorial Thermosphere Anomaly (ETA): Two crests around ±20-30° magnetic latitude and a trough at the magnetic equator in neutral temperature and density.

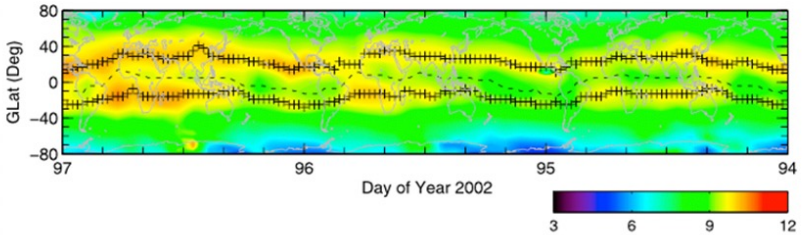

Figure: Neutral Mass Density at 400km from the CHAMP Satellite

Equatorial Ionization Anomaly (EIA): Two crests around ±10-20° magnetic latitude and a trough at the magnetic equator in electron density.

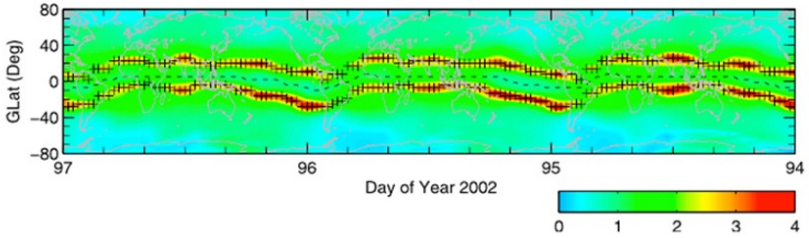

Figure: Electron Density at 400km from the CHAMP Satellite

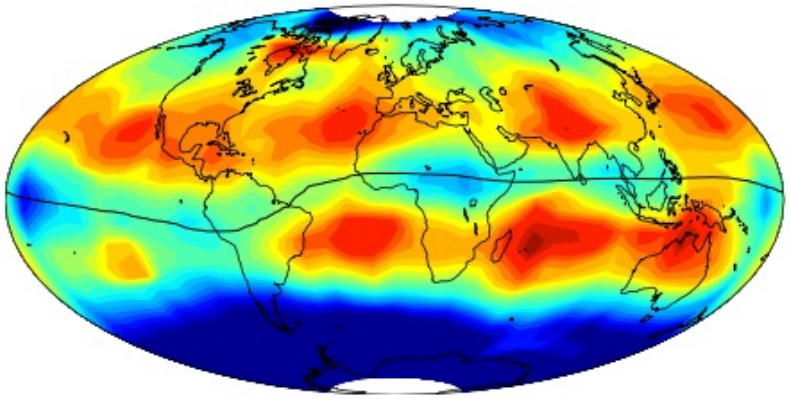

FIGURE 9.23

The spatial structure of the equatorial mass density anomaly (EMA) observed by CHAMP satellite at 400 km near equinox in 2002.

Jan 21 10:22(UTC)

Magnetospheric impacts on the ionosphere & thermosphere

Fig. 63 Model neutral wind variations driven by auroral heating (Fuller-Rowell et al. 2008). The model calculations show the northern component of the wind variation in color, starting at 3 hours after the initiation of an impulse auroral heating event. The vectors (*arrows*) show the total horizontal component, including the zonal wind component, represented according to the scale at the *upper right*

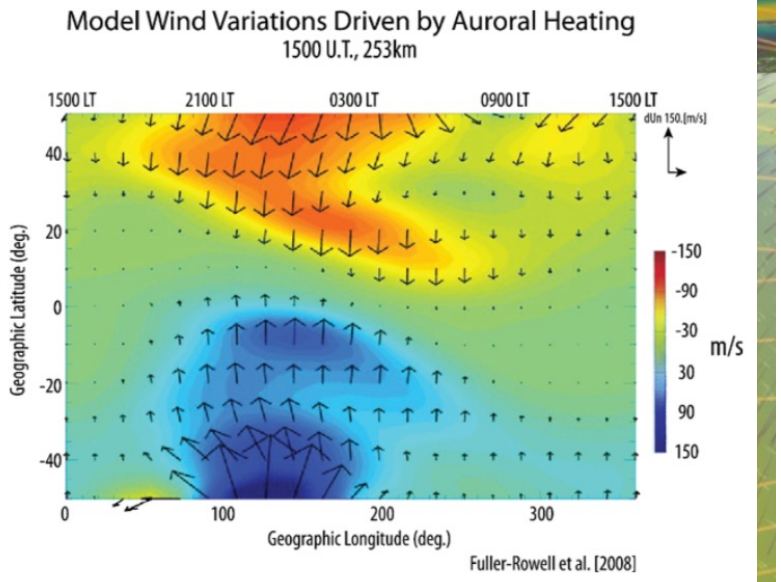

Fig. 65 Images of the earth at 130.4 nm during the daytime as observed by the VIS camera on the Polar satellite, showing the O/N_2 ratios during a quiet period before a storm on April 16, 2002 (*left*), and during a magnetic storm on April 19, 2002 (*right*). The data are provided by J. Sigwarth and J. Kozyra

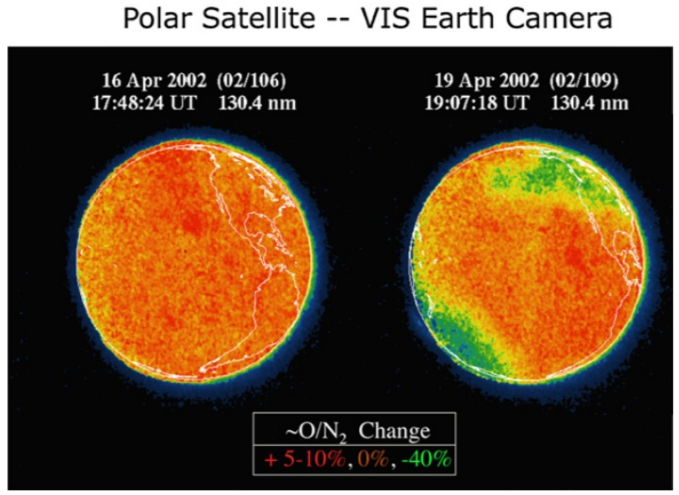

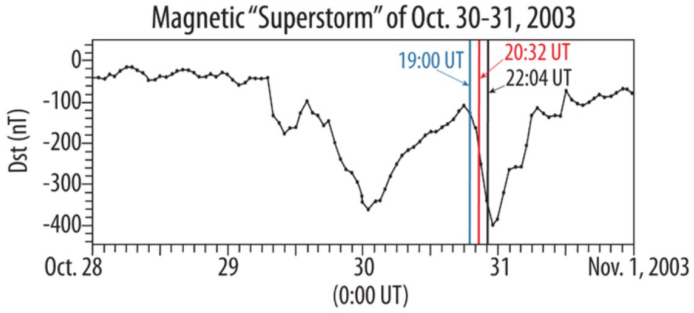

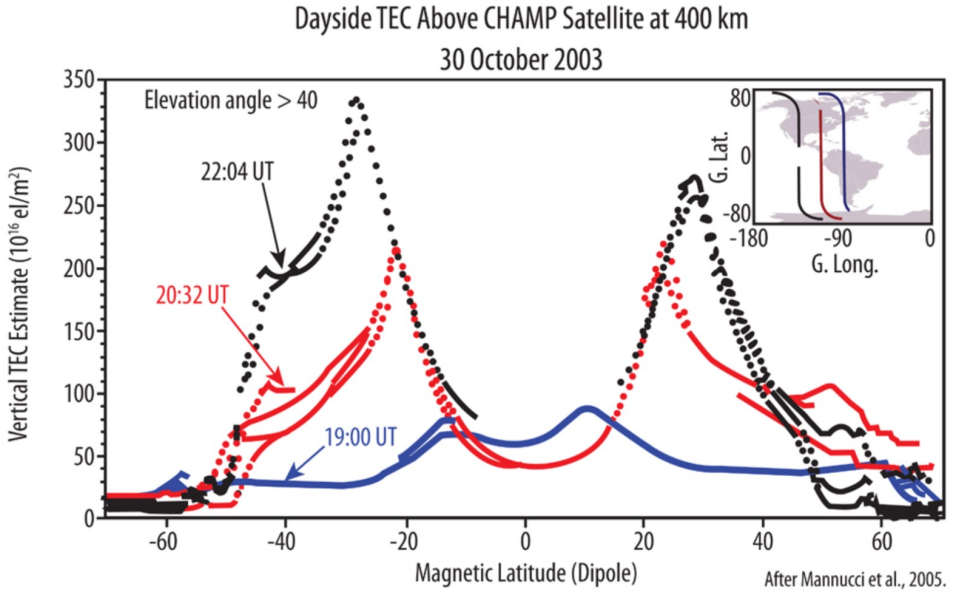

Fig. 70 The integrated electron content (corresponding to total electron content or TEC) as measured by the GPS instrument on the CHAMP satellite for altitudes above the CHAMP altitude of 400 km (*lower panel*). Data are shown for three orbits plotted as a function of magnetic latitude which correspond to times just prior to (*blue*) and after (*red* and *black*) the onset of a magnetic storm on October 30, 2003, as shown in the plot of Dst in the *upper panel*. The locations of the CHAMP orbits are shown in the upper right corner of the lower panel. The local times of these orbits range from 1230–1330 LT for latitudes within ±60 degrees. Points missing near the anomaly trough are due to the elevation angle cut-off (adapted from Mannucci et al. 2005)

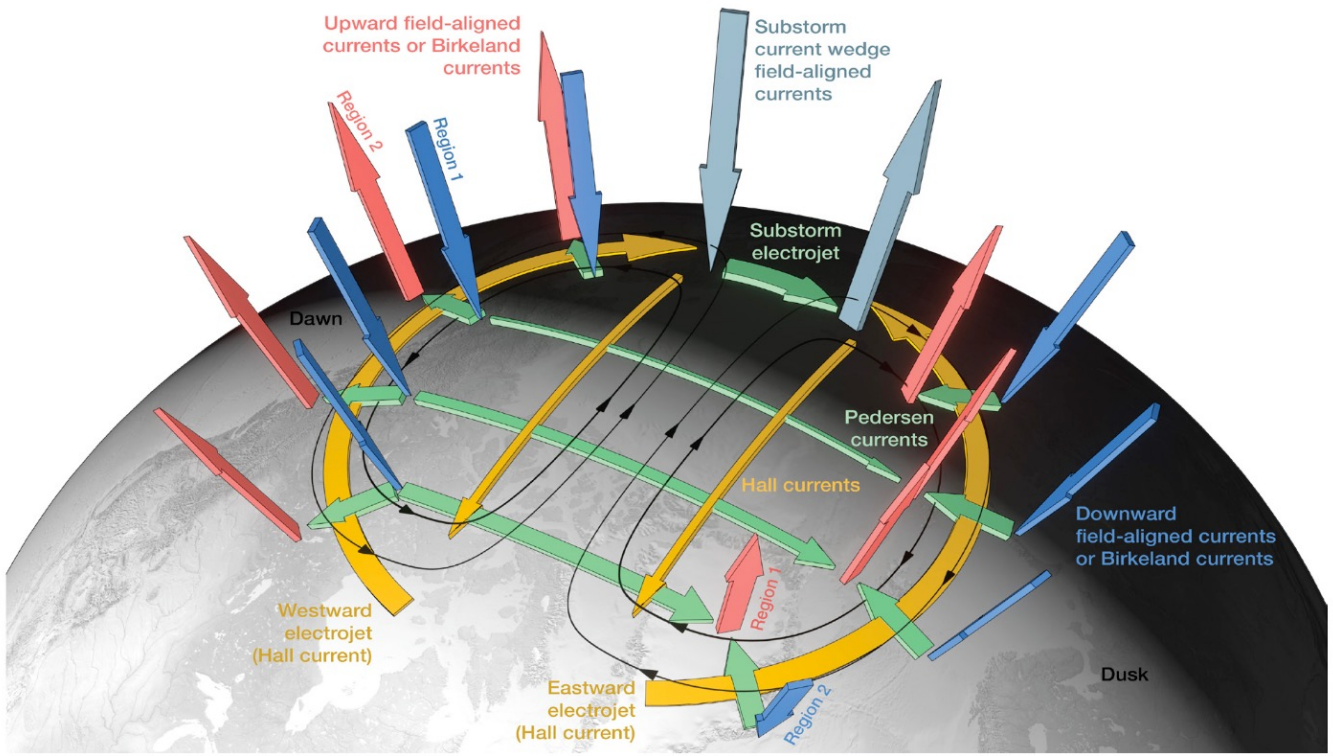

Figure 6 A schematic view of the high-latitude ionospheric current system (thick coloured arrows) superimposed to the ionospheric plasma convection pattern in the polar cap (thin black arrows) [figure: E. Doornbos, also in (Palmroth et al. 2020)].

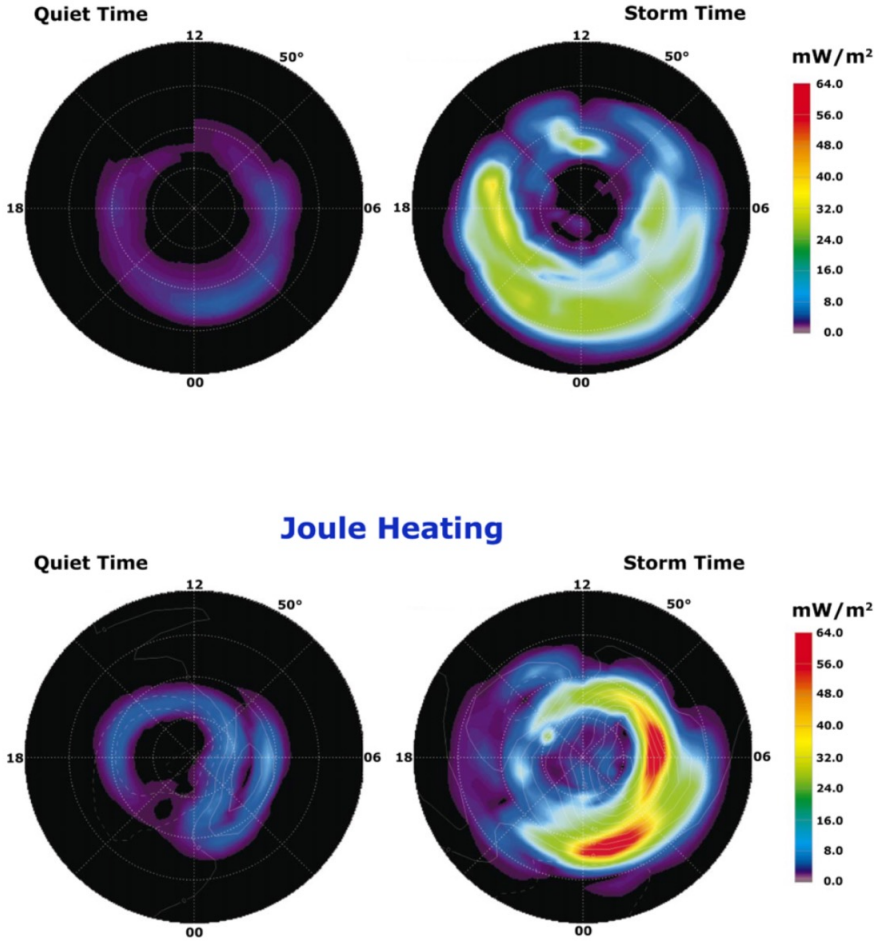

Fig. 62 Distributions in magnetic latitude and local time of the estimated auroral electron energy flux (*top*), the height-integrated Joule heating rate (*bottom*), and the electric potential (*bottom*, contours) above 50° magnetic latitude in the northern hemisphere for a quiet period on 1997 January 10: 0255 UT (*left*), and an active period at 1105 UT (*right*) on the same day. The electric-potential contour interval is 10 kV (Richmond and Lu 2000)

$$Heating: q_j = eN_e(\vec{v}_{i\perp} - \vec{u}_{n\perp}) \cdot \left(\vec{E} + \overrightarrow{u_n} \times \vec{B}\right)$$

$$Acceleration: \rho \frac{D\vec{u}}{Dt} = -\nabla p + \eta \frac{\partial^2 u}{\partial z^2} + \rho \vec{g} + \rho \nu_{n,i}(\vec{u}_i - \vec{u}) + 2\rho \vec{u} \times \vec{\Omega}_E$$

Jan 21 10:22(UTC)

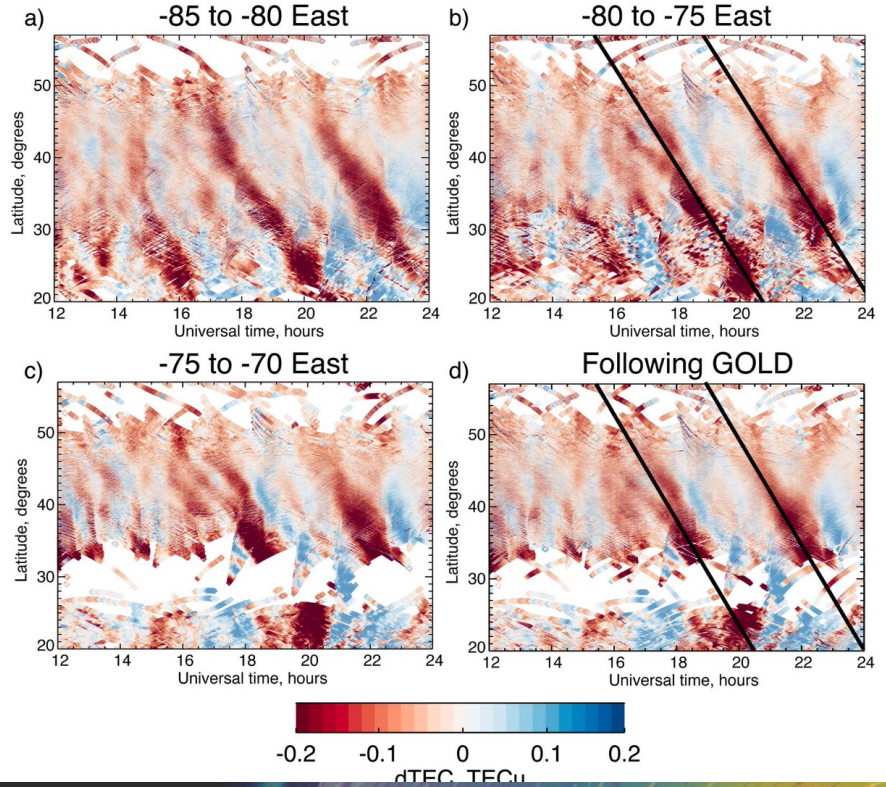
a)
-85 to -80 East
b)
-80 to -75 East
c)
-75 to -70 East
d)
Following GOLD
Latitude, degrees
Universal time, hours
-0.2
-0.1
0
0.1
0.2
dTEC, TECu

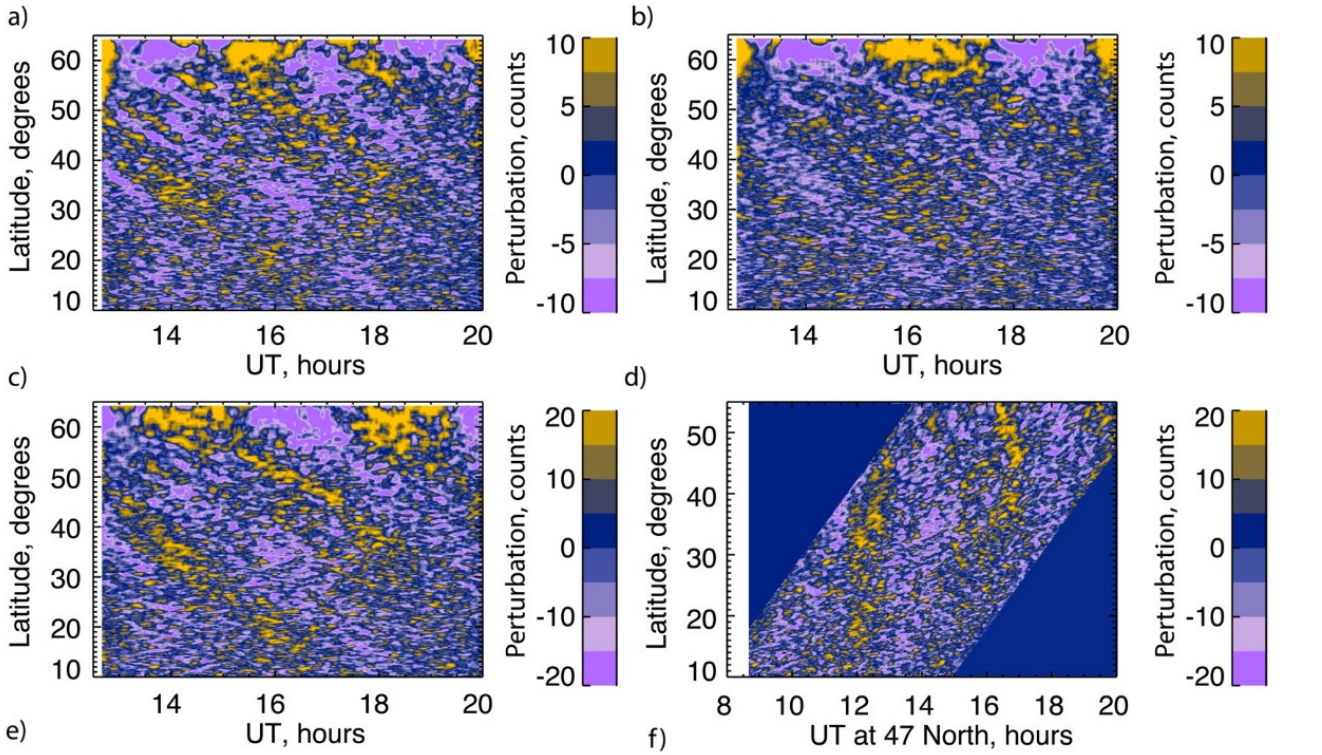
a)
b)
c)
d)
e)
f)
Latitude, degrees
UT, hours
Perturbation, counts
UT at 47 North, hours

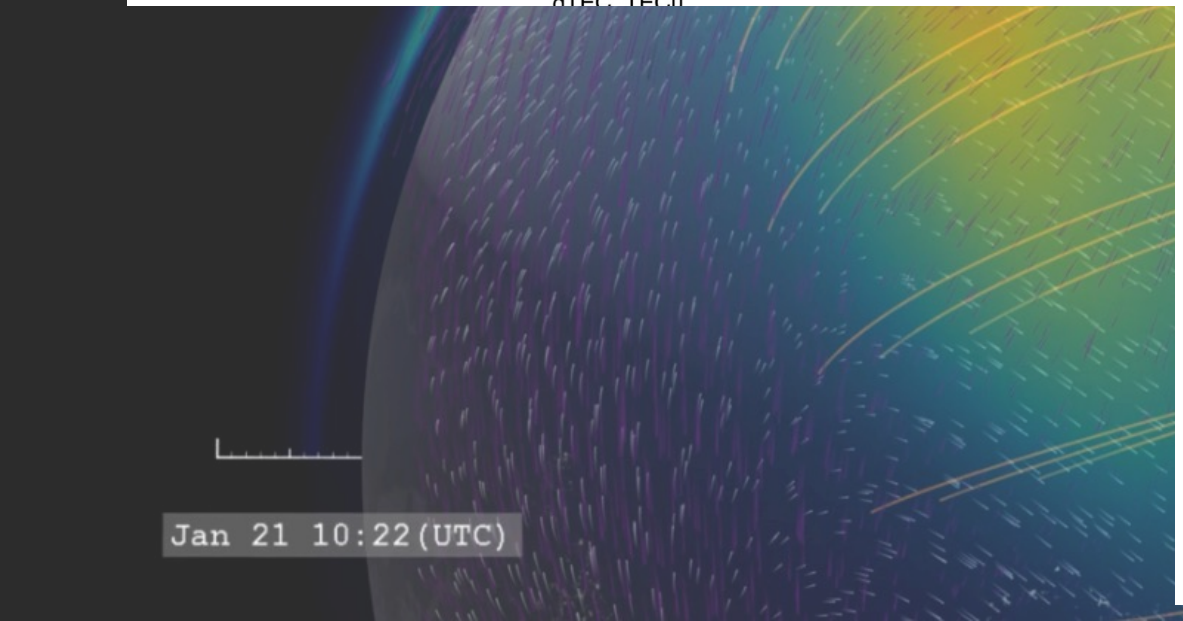
Jan 21 10:22(UTC)

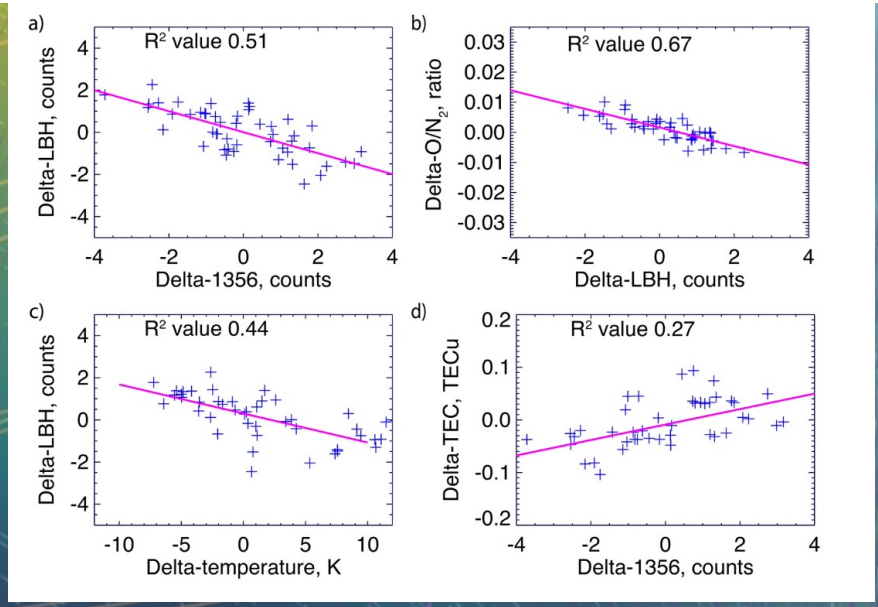
a)
R² value 0.51
Delta-LBH, counts
Delta-1356, counts
b)
R² value 0.67
Delta-O/N2, ratio
Delta-LBH, counts
c)
R² value 0.44
Delta-LBH, counts
Delta-temperature, K
d)
R² value 0.27
Delta-TEC, TECu
Delta-1356, counts

Citations

- ESA Daedalus RfA (2020). Earth explorer 10 candidate mission Daedalus report for assessment (RfA). Report for assessment, ESA Available at: https://esamultimedia.esa.int/docs/EarthObservation/EE10_Daedalus_Report-for- Assessment-v1.0_13Nov2020.pdf
- England, S. L., Meier, R. R., Frey, H. U., Mende, S. B., Stephan, A. W., Krier, C. S., et al. (2021). First results from the retrieved column O/N2 ratio from the Ionospheric Connection Explorer (ICON): Evidence of the impacts of nonmigrating tides. *Journal of Geophysical Research: Space Physics*, *126*, e2021JA029575. https://doi. org/10.1029/2021JA029575
- England, S. L., Englert, C. R., Harding, B. J., Triplett, C. C., Marr, K., Harlander, J. M., et al. (2022). Vertical shears of horizontal winds in the lower thermosphere observed by ICON. *Geophysical Research Letters*, *49*, e2022GL098337. https://doi. org/10.1029/2022GL098337
- England, S. L., Greer, K. R., Zhang, S.-R., Evans, S., Solomon, S. C., Eastes, R. W., et al. (2021). First comparison of traveling atmospheric disturbances observed in the middle thermosphere by Global-scale Observations of the Limb and Disk to traveling ionospheric disturbances seen in ground-based total electron content observations. *Journal of Geophysical Research: Space Physics*, *126*, e2021JA029248. https://doi. org/10.1029/2021JA029248
- B.G. Fejer, J.W. Jensen, S.-Y. Su, Quiet time equatorial F region vertical plasma drift model derived from ROCSAT-1 observations. J. Geophys. Res. **113**, A05304 (2008). doi:10.1029/2007JA012801
- Immel, T.J., Harding, B.J., Heelis, R.A. *et al.* 2021. Regulation of ionospheric plasma velocities by thermospheric winds. *Nat. Geosci.* Public access. DOI: 10.1038/s41561-021-00848-4
- Kil, H., S.-J. Oh, M. C. Kelley, L. J. Paxton, S. L. England, E. Talaat, K.-W. Min, and S.-Y. Su (2007), Longitudinal structure of the vertical E ! B drift and ion density seen from ROCSAT-1, Geophys. Res. Lett., 34, L14110, doi:10.1029/2007GL030018.
- Lei, J., J. P. Thayer, W. Wang, X. Luan, X. Dou, and R. Roble (2012), Simulations of the equatorial thermosphere anomaly: Physical mechanisms for crest formation, J. Geophys. Res., 117, A06318, doi:10.1029/2012JA017613
- Pfaff, R.F, The near-Earth plasma environment, 2012, Space Sci. Rev., doi:10.1007/s11214-012-9872-6
- G. Prölss, *Physics of the Earth's Space Environment: an Introduction* (Springer, Heidelberg, 2004
- Ionosphere-thermosphere interaction, in Cross-Scale Coupling and Energy Transfer in the Magnetosphere-Ionosphere-Thermosphere System, Ed: Y. Nishimura, O. Verkhoglyadova, Y. Deng and S-R. Zhang, Elsevier, ISBN: 978-0-12-821366-7, https://doi.org/10.1016/B978-0-12-821366-7.00007-X
- A.D. Richmond, G. Lu, Upper-atmospheric effects of magnetic storms: a brief tutorial. J. Atmos. Sol.-Terr. Phys. **62**, 1115–1127 (2000)
- Solomon, S. C., Andersson, L., Burns, A. G., Eastes, R. W., Martinis, C., McClintock, W. E., & Richmond, A. D. (2020). Global-scale observations and modeling of far-ultraviolet airglow during twilight. Journal of Geophysical Research: Space Physics, 125, e2019JA027645. https://doi.org/ 10.1029/2019JA027645
- G. Thuillier, R.H. Wiens, G.G. Shepherd, R.G. Roble, Photochemistry and dynamics in thermospheric in- tertropical arcs measured by the WIND Imaging Interferometer on board UARS: a comparison with TIE- GCM simulations. J. Atmos. Sol.-Terr. Phys. **64**, 405–415 (2002). doi:10.1016/S1364-6826(01)00109-2
- Yamazaki, Y., Arras, C., Andoh, S., Miyoshi, Y., Shinagawa, H., Harding, B. J., et al. (2022). Examining the wind shear theory of sporadic E with ICON/ MIGHTI winds and COSMIC-2 Radio 2 occultation data. *Geophysical Research Letters*, *49*, e2021GL096202. https://doi. org/10.1029/2021GL096202

Neutral wind impacts on the ionosphere

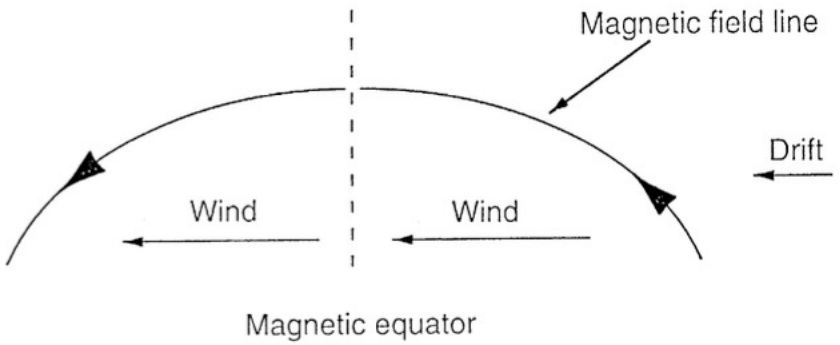

Fig. 2. Effect of a transequatorial neutral wind on the low latitudes ionosphere. The ionosphere plasma experiences a downward drift in the winter hemisphere.

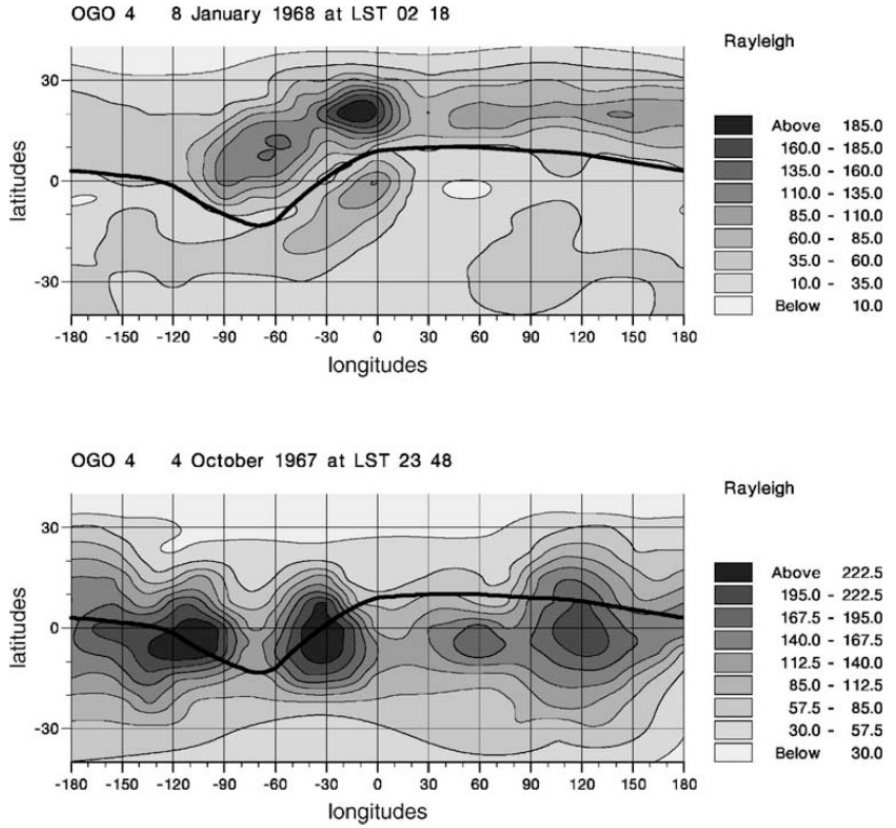

Fig. 1. Zenith emission lines (Rayleigh) shown as a function of latitudes and longitudes observed by the Orbital Geophysical Observatory (OGO 4). The black line is the magnetic equator. 8 January 1968 (top), 4 October 1967 (bottom).

Jan 21 10:22(UTC)

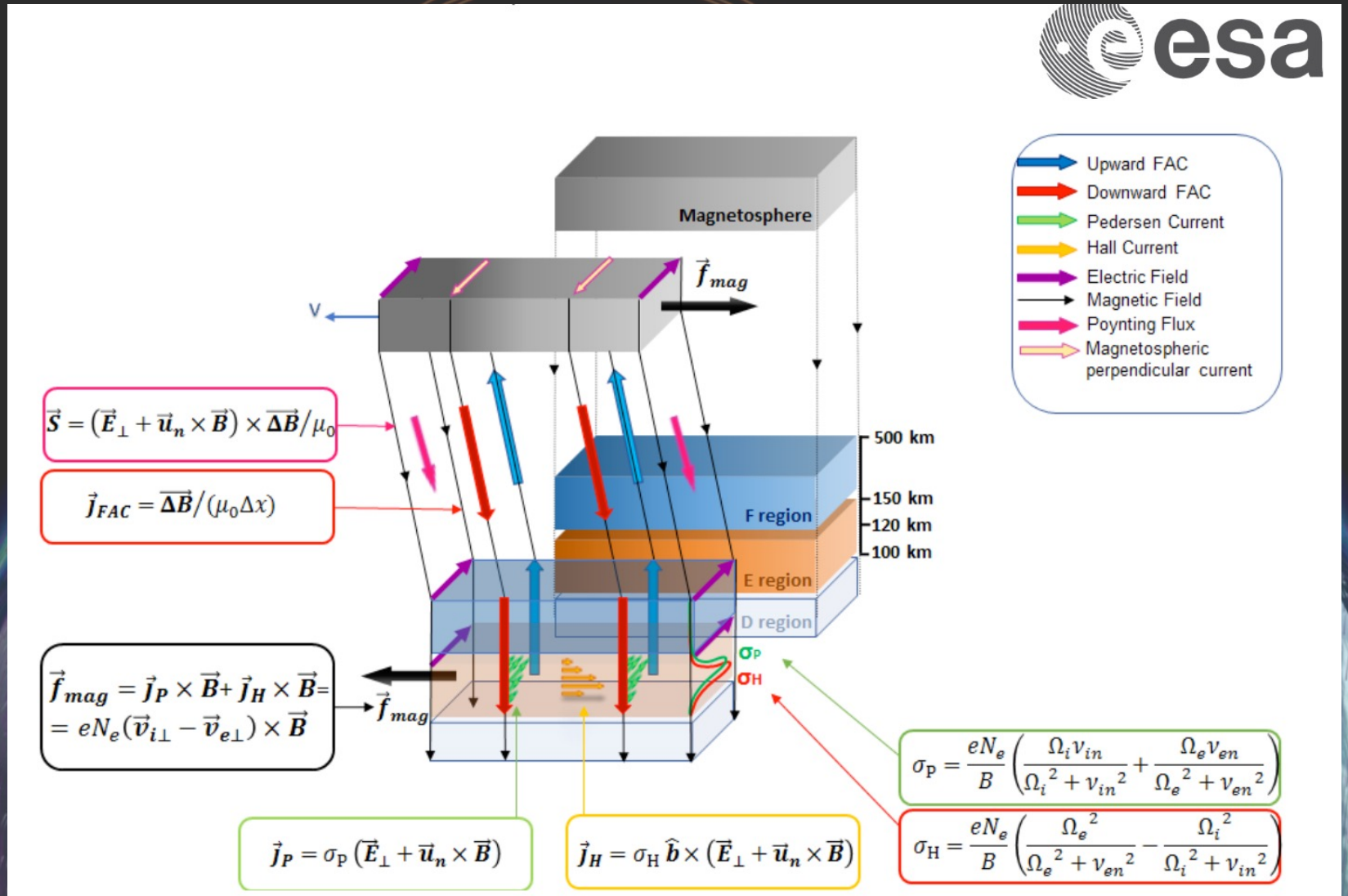

Figure 10 Schematic view of the high-latitude LTI electrodynamics, with equations describing field-aligned and horizontal currents, magnetic forcing, Poynting flux and expressions of the Hall and Pedersen conductivities [figure: T. Sarris, S. Tourgaidis]